Journal of the Korean Physical Society, Vol. 71, No. 10, November 2017, pp. 593∼607 Review Articles

Recent Advances of Flexible Hybrid Perovskite Solar Cells

Dong Hee Shin,* Jin Hyuck Heo* and Sang Hyuk Im†
Department of Chemical and Biological Engineering, Korea University, Seoul 02841, Korea

(Received 16 August 2017)

Recently, hybrid perovskite solar cells have attracted great interest because they can be fabricated to low cost, flexible, and highly efficient solar cells. Here, we introduced recent advances of flexible hybrid perovskite solar cells. We introduced research background of flexible perovskite solar cells in introduction part. Then we composed the main body to i) structure and properties of hybrid perovskite solar cells, ii) why flexible hybrid perovskite solar cells are important?, iii) transparent conducting oxide (TCO) based flexible hybrid perovskite solar cells, and iv) TCO-free transparent conducting electrode (TCE) based flexible hybrid perovskite solar cells. Finally, we summarized research outlook of flexible hybrid perovskite solar cells.

PACS numbers: 78.56.-a
Keywords: Hybrid perovskite, Solar cells, Flexible, TCO-free, Flexible substrate.
DOI: 10.3938/jkps.71.593

I. INTRODUCTION

Solar energy is one of the most abundant and sustainable energy source with minimal impact on environmental pollution compared to conventional energy sources such as fossil fuel and nuclear power. The electricity is the safest and most convenient energy form to maintain modern human life. Therefore, a solar cell is an ideal device for power generation because it can convert the solar light energy directly into electricity. However, the power generation cost and levelized cost of energy (LCOE) of solar cells are still more expansive than those of fossil fuel or nuclear power (see Table 1). To expand the utilization of solar cells, their power generation cost and LCOE should be further reduced. Accordingly, the types of solar cells can be classified to first, second, and third generation solar cells. Crystalline silicon-based solar cells are in first generation, [1–4] metal chalcogenide thin-film solar cells are in second generation, [5,6] and dye-sensitized, organic, and nanostructure-based solar cells [7–13] are in the third generation, respectively. Until now, the crystalline Si-based solar cells have been occupying most solar market, but they seem to have no sufficient margin to further reduce their power generation cost and LCOE because they require expansive vacuum process for high purity Si ingot and cheaper large area solution process cannot be applicable to produce Si solar cells. Hence, the solution processable third generation solar cells have been intensively studied to develop cost-effective solar cells with high efficiency.

The merit and demerit of solution processable third generation solar cells is shown in Fig. 1. The merit of organic solar cells is to high flexibility, cheap processability such as roll to roll (RTR) and color appearance. However, their expected limit of device efficiency is $\sim$ 15% due to significant potential loss to dissociate the generated excitons, which is too low value to compete with conventional Si solar cells for power generation. The vacuum processed metal chalcogenide thin-film solar cells such as CIGS(e), (CuInGaS(e)), and CdTe can exhibit comparable efficiency with the Si solar cells, but their competitiveness is still weaker than the Si solar cells in terms of power generation cost. Therefore, the solution processable thin-film solar cells have been extensive studied by using ink or dispersion, but currently their efficiency is below 15% possibly due to many interface traps in grain boundaries. Recently, the quantum dot (QD) solar cells have been studied intensively because their theoretical maximum efficiency in single junction solar cells is $\sim$ 41% by utilization of multiple exciton generation, whereas the other single junction solar cells have $\sim$ 31% of theoretical limit. However, currently their record efficiency is below 15% because several tens or hundreds of QD-layers must be deposited to fully absorb the light so that the extreme number of interface are necessarily formed, which might cause interface traps. Unlike aforementioned solar cells, the sensitized solar cells are constructed to electron conductor (n), sensitizer (i), and hole conductor (p) so that high efficiency can be achievable by using relatively impure materials with cheaper price. Accordingly, the sensitized type solar cells will be good to realize cost-effective high performance solar cells.

*These two authors have equally contributed to this work.
†E-mail: imromy@korea.ac.kr

Table 1. Historical and projected LCOE of US EIA (Energy Information Administration). (Data from: https://en.wikipedia.org/wiki/Cost_of_electricity_by_source)

Estimate in $/MWh		Coal conventional	NG combined cycle		Nuclear advanced	Wind		Solar	
of year	for year		conventional	advanced		onshore	offshore	PV	CSP
2010	2016	100.4	83.1	79.3	119.0	149.3	191.1	396.1	256.6
2011	2016	95.1	65.1	62.2	114.0	96.1	243.7	211.0	312.2
2012	2017	97.7	66.1	63.1	111.4	96.0	N/A	152.4	242.0
2013	2018	100.1	67.1	65.6	108.4	86.6	221.5	144.3	261.5
2014	2019	95.6	66.3	64.4	96.1	80.3	204.1	130.0	243.1
2015	2020	95.1	75.2	72.6	95.2	73.6	196.9	125.3	239.7
2016	2022	NB	58.1	57.2	102.8	64.5	158.1	84.7	235.9
2017	2022	NB	58.6	53.8	96.2	55.8	NB	73.7	NB
Nominal change 2010 - 2017		NB	−29%	−32%	−19%	−63%	NB	−81%	NB

CSP = concentrated solar power
NB = Not built (No capacity additions are expected.)

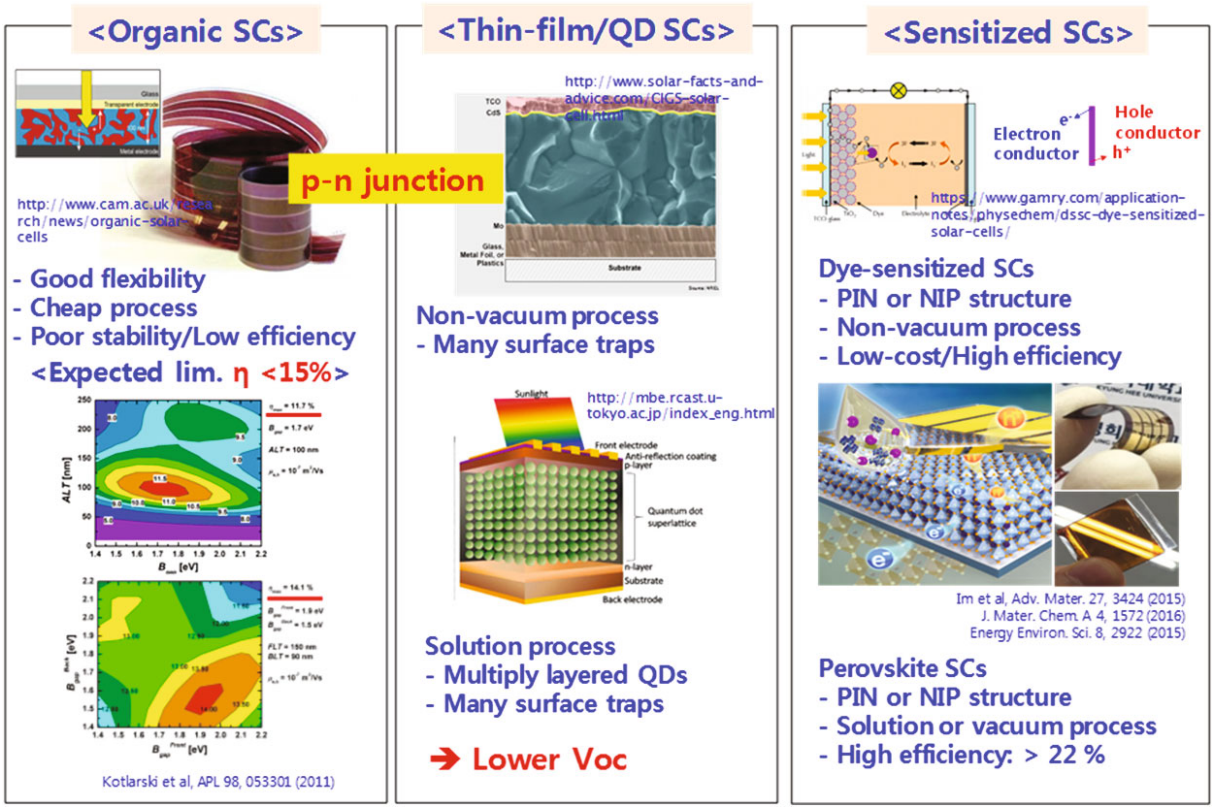

Fig. 1. (Color online) The advantages and disadvantages of solution processable third generation solar cells

Very recently, the hybrid perovskite solar cells surprised the photovoltaic community with remarkable performance and rapid development for five years. The hybrid perovskite materials have unique properties such as high absorptivity due to direct bandgap, high open circuit voltage (V_{oc}) by small exciton binding energy, convenient bandgap tunability by composition and structure engineering, and solution processability so that their record efficiencies reached over 22% [14–18]. To date, the needs for independent power generation are gradually growing because the energy consumptions in buildings, cars, smart phones, pablet PCs, wearable devices, and IOTs. Therefore, the hybrid perovskite solar cells are ideal power generation system for future energy de-

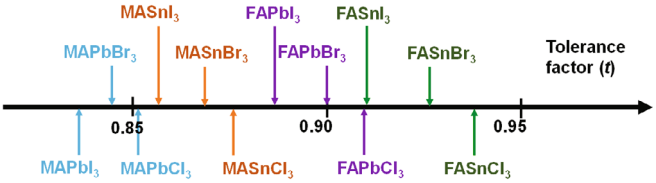

Fig. 2. (Color online) Tolerance factors (t) of a series of halide perovskites. Reprinted from Ref. [44].

mands requiring flexibility and high performance.

In general, the device architecture of perovskite solar cells can be classified to *n-i-p* (normal) and *p-i-n* (inverted) type devices in terms of what type of materials are placed on the transparent conducting electrode (TCE) such as fluorine doped tin oxide (FTO) or indium tin oxide (ITO). The transparent conducting oxide (TCO) coated glass substrates are effective barriers to water and oxygen penetration, but high-temperature processes are required to produce high-efficiency solar cells [19–23]. However, the main disadvantage of TCO based glass substrate is the rigidity, weight and vulnerability that limits the possibility of integrating photovoltaic devices into large-scale and roll-to-roll modules. Instead, flexible substrates can be easily molded into a variety of shapes, and thin-film photovoltaic panels containing these substrates can be integrated with a variety of shapes and sizes of infrastructures for innovative energy generation products.

Hence, many groups have focused on designing low-cost, lightweight, and mechanically flexible thin-film photovoltaics, enabling large-scale implementations of portable, miniaturized and RTR devices [24–36]. To date, wealth studies on the new hole transporting materials (HTMs) and electron transporting materials (ETMs) have been done to develop flexible perovskite solar cells, as well. Accordingly, we would like to discuss recent advances in flexible hybrid perovskite solar cells.

II. STRUCTURE AND PROPERTIES OF HYBRID PEROVSKITE SOLAR CELLS

1. Structure of hybrid perovskite materials

Halide hybrid perovskites can be divided into alkali metallic halide perovskites and organometallic halide perovskites. The first organic-inorganic hybrid perovskite was synthesized 36 years ago by Dieter Weber [37, 38]. Mitzi and colleagues explain the structure and properties of the hybrid perovskite [39,40]. The organometallic halide perovskite is sufficient to achieve good photoconversion performance as a thinner absorber layer owing to superior light harvesters.

Organolead halide perovskite materials have attracted considerable interest as light harvesters for hybrid solar

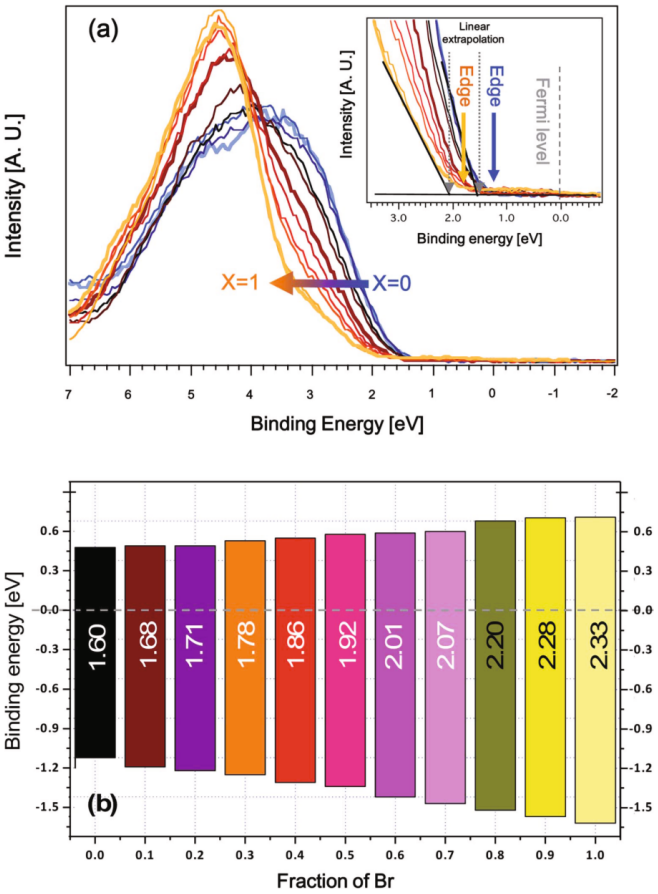

Fig. 3. (Color online) Valence levels spectra of the $MAPb(I_{1-x}Br_x)_3(Cl)_y$ series measured by XPS. Inset: the upper valence band including a linear extrapolation and an indication of the experimental spectral edge for the $MAPbI_3$ and $MAPbBr_3$ (b) Schematic drawing of the $MAPb(I_{1-x}Br_x)_3(Cl)_y$ energy levels determined from (a). Reprinted from Ref. [56].

cells due to their high adsorption coefficients [41] and charge mobility [40]. The perovskite material has a specific crystal structure as ABX_3 formula. The larger A cations occupy cuboctahedral sites shared with twelve X anions, while smaller B cations stabilize at octahedral sites shared with six X anions. Organic-inorganic halide perovskite materials are commonly used in solar energy applications. Wherein the larger A cation is organic ammonium: typically methylammonium ($CH_3NH_3^+$, MA) or formamidinium ($H_2NCHNH_2^+$, FA), the X anion is halogen: generally I^- and Br^- and Cl^- are also commonly used., and the cations B is divalent metal: commonly Pb is used for efficient solar cells. The formation of perovskite structure is estimated by the Goldschmidt tolerance factor (t): [42]

$$t = (r_A + r_X)/\left[\sqrt{2}(r_B + r_X)\right], \quad (1)$$

where r_A, r_B, and r_X are radius of the A, B, and X ions, respectively. In general, the cubic structure is

Table 2. Temperature-dependent structural characteristics of $CH_3NH_3PbBr_3$ and $CH_3NH_3PbI_3$. Reprinted from Ref. [59].

Phase	Temperature (K)	Crystal structure	Dielectric Constant (ε')	Electronic bandgap (E_g)
$CH_3NH_3PbBr_3$			25.5 (ionic), 4.8 (electronic)	2.3
A	> 236.9	Cubic		
β	155.1 - 236.9	Tetragonal		
γ	149.5 - 155.1	Tetragonal		
δ	< 144.5	Orthorhombic		
$CH_3NH_3PbI_3$			28.8 (ionic), 6.5 (electronic)	1.5
α	> 327.4	Cubic		
β	162.2 - 327.4	Tetragonal		
γ	< 162.2	Orthorhombic		

$0.89 < t < 1$ for oxide perovskite [43] and $0.85 < t < 1.11$ for halide perovskite [44]. Cubic symmetry provides optimum electronic properties due to the high level of ionic bonding. If the crystal components outside the ideal tolerance range are not matched, arcuate tilting will occur which can affect the electronic properties, as shown in Fig. 2. For example, if $t < 1$, the $B - X$ bond is compressed and the $A - X$ bonds tension compensates for excess space (void). The octahedral rotation accommodates this induced stress and reduces the symmetry and tilt of the BX_6 octagon. If $t > 1$, a higher degree of symmetry occurs as a result of a larger A or smaller B, resulting in a more stable hexagonal structure. In addition, the perovskite can have different dimensions depending on the part size.

2. Properties of hybrid perovskite materials

The remarkable performance of hybrid perovskites relies on their unique material properties. Hybrid perovskites show strong light absorption, tunable bandgap, small exciton binding energy, long charge carrier's diffusion length, ambipolar charge transport, and high carrier mobility [45–55]. The straightforward adjustment of electronic and optical properties of hybrid perovskites is also very attractive in terms of material design. The absorptivity of hybrid perovskites is very strong so that very thin hybrid perovskite layer can effectively absorb the light, thereby charge collection efficiency can be improved [47, 48, 52]. Generally, the thickness of hybrid perovskite layer is below 500 nm, which is much thinner than the thickness of conventional chemical compound thin-film solar cells. $MAPbI_3$-based devices typically achieve absorption up to the end of the red region of the spectrum of about 800 nm. Figure 3 shows the valence band shift is larger than that of the conduction band shift, effectively reducing the band gap. The absorption spectra of $MAPbI_3$ and $MAPbI_{3-x}Cl_x$ are nearly identical, with an onset located at approximately 800 nm, and $MAPbI_{3-x}Br_x$ exhibits absorption up to 700 nm at increased energy [21, 47, 56, 57]. $MAPbI_3$ exhibits a

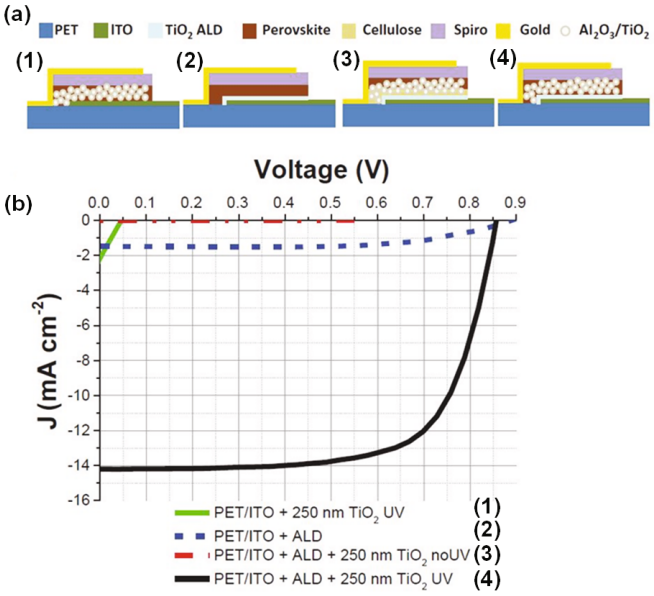

Fig. 4. (Color online) (a) Cross-section schematics of the architecture we fabricated. (b) J-V curves of the best small area cells measured at 1 sun: (1) light green continuous line is for a cell without ALD compact layer, (2) blue dashed line for a cell with ALD compact layer and without scaffold, (3) red dotted-dashed line for a cell with ALD compact layer and TiO_2 without UV irradiation, and (4) black continuous line for a cell with ALD compact layer and UV irradiated TiO_2. Reprinted from Ref. [77].

sharp absorption onset expression with an Urbach energy of 15 meV [58]. The optical absorption increases exponentially beyond the 10^4 cm^{-1} in the region over the band gap energy without the optically detected deep state. The lack of detectable sub-bandgap absorption below 1.5 eV of photoelectron energy for the perovskite implies a promising candidate for a serial device. The energy band alignment of a commonly used hybrid perovskite material is shown in Fig. 3.

$MAPbBr_3$ and $MAPbI_3$ perovskite materials in solar cells are known to have reversible thermochromism and high dielectric constants by large ionic polarization,

Table 3. Photovoltaic parameters of flexible perovskite solar cells by 2017.

Year	Device structure	V_{oc} (V)	J_{sc} (mA/cm^2)	FF (%)	PCE (%)	Ref
2013	PET/ITO/PEDOT:PSS/$MAPbI_{3-x}Cl_x$/PCMB/TiO_x/Al	0.88	14.4	51	6.40	[87]
	PET/Ag/PEDOT:PSS/PolyTPD/$MAPbI_3$/PCBM/Au	1.04	14.30	47	7.00	[93]
2014	PEN/ITO/ $MAPbI_{3-x}Cl_x$/Spiro-OMeTAD/Ag	0.95	21.40	60	12.20	[77]
	PET/ITO/$MAPbI_3$/Spiro-OMeTAD/Ag	1.03	13.40	73	10.20	[83]
	Ultra thin Ag/Spiro-OMeTAD/$MAPbI_3$/mp-TiO_2/TiO_2/Ti	0.88	9.50	73	6.15	[31]
2015	PET with Ni mesh/transparent conductive adhesive/ PEDOT:PSS/Spiro-OMeTAD/$MAPbI_{3-x}Cl_x$/Al_2O_3/TiO_2/Ti	0.98	17.0	61	10.3	[97]
	PEN/ITO/ZnO/$MAPbI_3$/PTAA/Au	1.10	18.7	75	15.4	[84]
	NOA63/PEDOT:PSS/$MAPbI_{3-x}Cl_x$/PCBM/EGaIn	0.94	15.5	70	10.2	[94]
2016	Colorless PI/ITO/$MAPbI_3$/PCBM/Au	1.10	17.6	79	15.2	[95]
2017	PEN/Graphene/MoO_3/PEDOT:PSS/$MAPbI_3$/C_{60}/PCB/LiF/Al	1.00	21.7	78	16.8	[104]

thereby exhibiting small exciton binding energies (BE), owing to the generation of Wannier-type excitons, as shown in Table 2 [59]. In the case of the $MAPbI_3$ and $MAPbBr_3$ perovskite material, it is known that the exciton BE at room temperature has a value of ~ 30 and ~ 76 meV. So that free electrons and holes can be generated at room temperature. Therefore, a perovskite type hybrid solar cell can obtain a high V_{oc} by a small exciton BE. Carrier diffusion lengths (L_n) up to 100 nm for both electrons/holes of $MAPbI_3$ and the L_n in the mixed halide $MAPbI_{3-x}Cl_x$ exceed 1000 nm in have been reported by transient photo-luminescence (PL) measurements [51,60].

In solar cell, when a light absorber (donor or p-type material) receives sunlight, the electrons in the current-carrying band are transferred to the conduction band to form an electron-hole pair. In this case, the generated electron-hole pairs are strongly coupled to each other due to the coulomb force, so that the net charge has a value of zero, which is called an exciton. Therefore, the generated excitons are randomly diffused in the solar cell device in which the electric field is generated, and the excitons reaching the p-n junction are separated into free electrons and free holes while consuming the exciton binding energy. The free electrons and the free holes are moved to the electrodes, respectively, to generate electricity along the external circuit. Generally, organic solar cells require an energy of $\sim 10kT$ (~ 250 meV) to separate excitons into free charges due to the low dielectric constant of organic materials, resulting in an open-circuit voltage loss of ~ 0.5 V or more. Therefore, the theoretical efficiency of the organic solar cell is as low as 15% or less. On the other hand, inorganic solar cells require exciton separation energy of $\sim 2kT$ (~ 50 meV) due to a large dielectric constant, so that they have a low open-circuit voltage loss of > 0.2 V, which makes it possible to manufacture solar cells with high efficiency. The hybrid perovskite solar cells have very high open circuit voltages due to their high dielectric constant and very small exciton binding energy values. Therefore, it is expected that the hybrid perovskite material is capable of generating free electrons and free holes at room temperature and both electrons and holes can move well under an electric field.

III. WHY FLEXIBLE HYBRID PEROVSKITE SOLAR CELLS ARE IMPORTANT?

With the advancement of science, people are looking for more comfortable electronic devices that are flexible, foldable, and wearable. Until now, the power conversion efficiency (PCE) of the perovskite-based solar cell has reached $\sim$ 22% [17, 18, 20, 47, 61–63]. The enormous amount of perovskite for practical application in various kinds of optoelectronic devices including solar cells. Perovskite solar cells can be used as an effective power source for flexible, portable and wearable appliances [64–67]. Perovskite materials have a high extinction coefficient for visible and low exciton BE, making them an excellent light harvester for photovoltaic applications in the nanoscale. The advantage of perovskite solar cells is their ability to reduce energy duplication in most excitonic solar cells, such as organic photovoltaic, with high output voltages close to the optical bandgap. Perovskite has ambipolar nature, meaning it can act as an electron or hole transporter, allowing for a versatile design of the device architecture. In addition, flexible perovskite solar cell is attracting more attention because it allows the compatibility of roll-to-roll continuous solar devices that can contribute significantly to the cost of producing large-area modules [68]. Furthermore, they can improve the power conversion density according to the curve [69, 70]. In recent years, studies on perovskite solar cells have been actively conducted with flexible substrates and electrodes. As shown in Table 3, a brief overview of the performance of flexible perovskites is shown. We also describe the structure and efficiency of flexible solar cells.

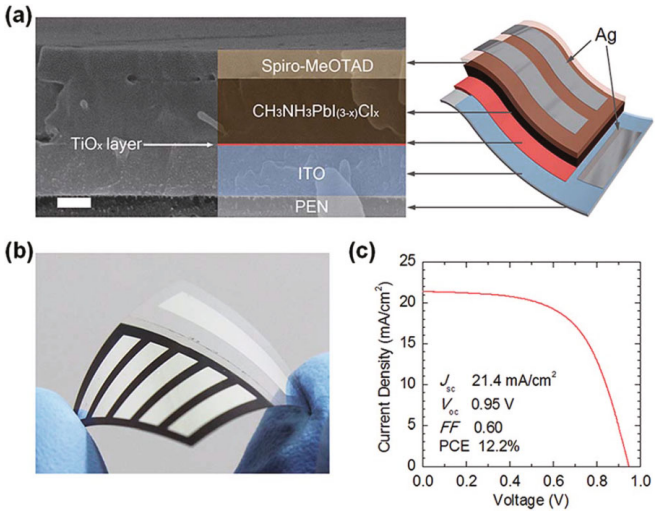

Fig. 5. (Color online) (a) Cross-sectional SEM image of the $MAPbI_{3-x}Cl_x$ perovskite planar heterojunction flexible solar cell and schematic of the flexible device structure. The scale bars all indicate 200 nm. (b) An actual bent image of a flexible perovskite solar cell. (c) J-V characteristics measured under AM 1.5G for the best performing $PEN/ITO/TiO_x/MAPbI_{3-x}Cl_x$/spiro-MeOTAD/Ag flexible device. Reprinted from Ref. [56].

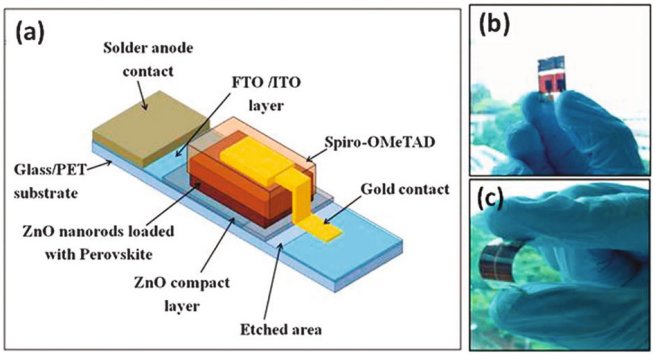

Fig. 6. (Color online) (a) Schematic of the architecture for the perovskite device. Real images of (b) device on the FTO substrate, and (c) device on the flexible PET/ITO substrate.

IV. TCO BASED FLEXIBLE HYBRID PEROVSKITE SOLAR CELLS

1. *n-i-p* type flexible hybrid perovskite solar cells

A. TiO_2 based flexible hybrid perovskite solar cells

In general, solar cell architectures with a mesostructured TiO_2 or Al_2O_3 support generally exhibit excellent efficiency and stability on glass substrates when annealed at high temperatures [71–75]. However, the high-temperature heat treatment process is inevitable for application to a flexible substrate. Therefore, low-temperature process is required to produce a mesoporous nanocrystalline material well-connected to a high-quality compact hole barrier layer. Recently, Zardetto *et al.* proposed a UV irradiation process for tailor-made TiO_2 nanoparticle pastes for the production of an efficient flexible dye-sensitized solar cell. The atomic layer deposition (ALD) method has also been used to fabricate thin and uniform layers at low temperatures in many photovoltaic technologies. The plasma approach offers several advantages. Compared with the conventional heat treatment method, it is possible to deposit a high quality film in particular, and is possible in view of a lower pinhole density in a temperature range compatible with the conductive plastic substrate [76]. Recently, Giacomo *et al.* have fabricated compact TiO_2 layer/scaffold at low temperature (150 °C) by UV irradiation combined with ALD to form a flexible perovskite solar cell on an ITO coated polyethylene terephthalate (PET) as shown in Fig. 4 [77]. As a result, the efficiency of 8.4% was achieved from the current density-voltage (J-V) curve of the device with area of 0.12 cm^2 under 1 sun. After developing the most efficient compact layer/scaffold combinations at the cell level, they have achieved 3.1% efficiency by manufacturing flexible photovoltaic modules consisting of four series-connected cells on 5.6 × 5.6 cm PET/ITO substrates. The apparatus also showed excellent mechanical resistance to bending tests and confirmed that the initial PCE was maintained after 100 bending cycles at a large radius of curvature. However, at a smaller radius (0.5 mm), cracking of ITO leads to an increase in sheet resistance, leading to a decrease in PCE. Figure 5 also shows that Kim *et al.* produced a highly bendable mixed halogenated perovskite solar cell with an excellent PCE of 12.2% based on a polyethylene naphthalate (PEN)-deposited ITO flexible substrate [78]. In this study, ∼ 20 nm thick amorphous TiO_x sublayer was deposited on the PEN/ITO substrate using plasma enhanced-ALD. They observed a high photocurrent density (J_{sc}) of more than 20 mA/cm^2 with recombination blocking and electron transport properties due to TiO_x layer fabrication. Furthermore, PCE proved that it did not change after 1000 cycles of bending test under conditions of 10 mm bending radius.

B. ZnO based flexible hybrid perovskite solar cells

ZnO is one of candidates replacing TiO_2 and Al_2O_3 due to its proper band energy levels and excellent electron transport properties [79–81]. In addition, the ZnO nanoparticle layer can be easily deposited by spin coating and is ideal for depositing on heat-sensitive substrates because no heat treatment is required. Based on this, Kumar *et al.* fabricated $MAPbI_3$ perovskite solar cells using spiro-OMeTAD and ZnO nanorods/planar ZnO as the hole transport layers (HTL) and electron trans-

Table 4. Parameters for ITO/ZnO/$MAPbI_3$/spiro-OMeTAD/Ag solar cells fabricated with various thicknesses of ZnO. Reprinted from Ref. [83].

No. of layers	ZnO thickness (nm)	V_{oc} (V)	J_{sc} (mA/cm^2)	FF (%)	PCE (%)
0	0	0.46	16.5	31.7	2.4
1	10	0.99	18.0	62.4	11.1
3	25	1.01	20.5	69.6	14.4
5	40	1.01	18.9	70.0	13.3
8	70	1.01	18.4	69.5	12.9

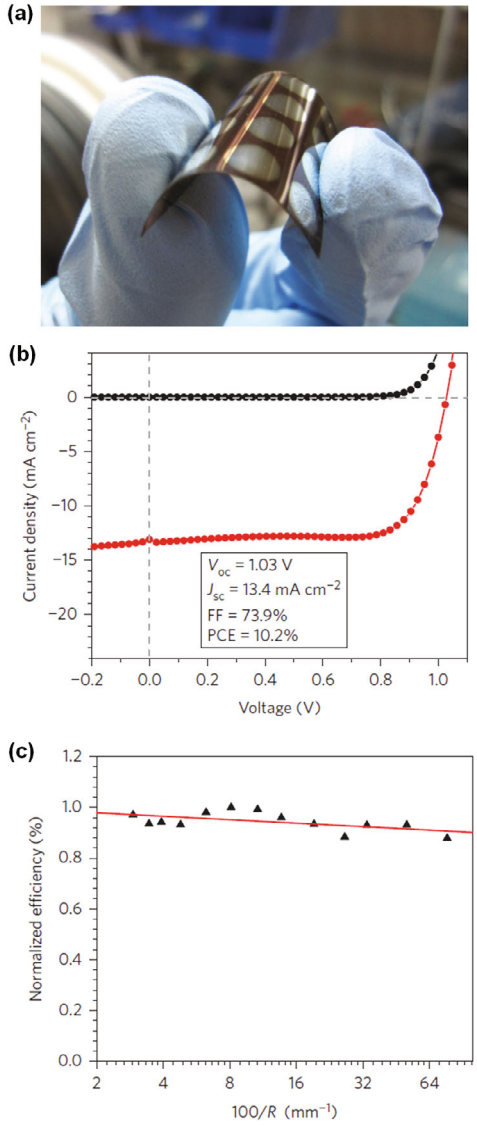

Fig. 7. (Color online) (a) Photograph of an ITO/ZnO/$MAPbI_3$/spiro-OMeTAD/Ag device prepared on a flexible PET substrate. (b) Typical J-V curves of solar cells under dark (black line) and illumination (red line). (c) Normalized PCE (measured on a flat device) after first bending the substrate around a cylindrical object of the specified radius. Reprinted from Ref. [83].

port layers (ETL), respectively, with PCE of 2.62% on flexible PET/ITO-based substrates at low temperature (< 100 °C), as shown in Fig. 6 [82]. In general, the performance of devices fabricated on FTO/glass is superior to those fabricated on ITO/PET, which is attributed to the inherent sheet resistance of the substrates used. However, the anorod device (PCE = 8.90%) showed higher PCE in the FTO than the planar device (PCE = 5.54%). They found that the less irregular perovskite overlays found in the nanorod samples increased the fill factor (FF) by allowing the formation of thinner spiro-OMeTAD layers. For this reason, this improvement in nanorod devices compared to planar devices has also been observed on ITO/PET substrates. In this study, the ZnO nanorod form promotes more charge collection and increased perovskite loading with a uniform perovskite layer and improves PCE compared to planar ZnO devices. Kelly *et al.* also fabricated $MAPbI_3$ perovskite solar cell with ZnO as the ETL and achieved PCE higher than 10% on flexible substrates under 1 Sun [83]. They prepared different ETLs with varying thicknesses from 0 to 70 nm to investigate the effect of ZnO layer thickness on device performance. As shown in the data without ZnO layer (Table 4), the device produced very low FF and V_{oc} due to the increased charge recombination on the ITO surface and consequent lower shunt resistance. Incorporation of a very thin (10 nm) ZnO layer into the device substantially improved both V_{oc} and FF and resulted in PCE exceeding 14% with a ZnO thickness of 25 nm. The device performance was not improved even though the thickness of the ZnO layer was further increased (Table 4). The optimized ZnO thickness for flexible device fabrication was taken as 25 nm. The bending test of the flexible device is shown in Fig. 7. The flexible device exhibits good performance even after repeated bending to lower the radius of curvature. When the ITO/PET substrate is bent to a radius of curvature to the point where it can no longer recover its original shape, the device performance is reduced by 15% from the original. More recently, Heo *et al.* introduces the planar $MAPbI_3$ perovskite flexible solar cell that can process high efficiency low temperature solution using ZnO ETL. The best solar cell device shows 1.13/1.13 V V_{oc}, 20.1/20.1 mA/cm^2 J_{sc}, 77/78% FF, and 17.5/17.7% PCE for the forward/reverse scan directions, respectively. The statistical deviation of the mean PCE for 40 solar cells shows that

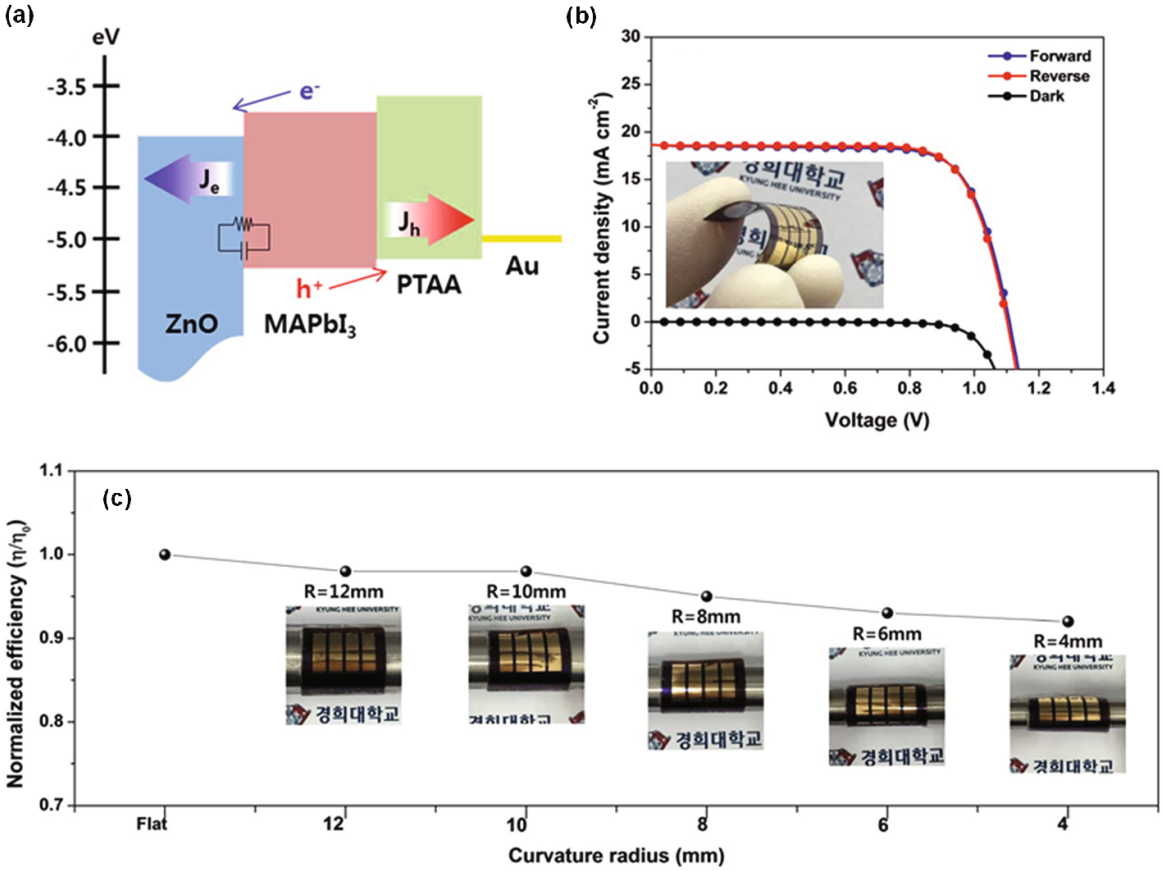

Fig. 8. (Color online) (a) Schematic band energy diagram of ZnO electron conductor based $MAPbI_3$ planar perovskite hybrid solar cells (b) J-V curves of PEN/ITO/ZnO/$MAPbI_3$/PTAA/Au flexible solar cells under illumination of 1 Sun: inset = photograph of the corresponding flexible solar cells, and (c) normalized power conversion efficiency (η) of PEN/ITO/ZnO/$MAPbI_3$/PTAA/Au flexible solar cells with bending radius. Reprinted from Ref. [84].

a PCE of $15.96 \pm 1.07\%$ is achieved [84]. Moreover, the efficiency of the flexible device did not show any significant degradation after bending at 12-4 mm of bending radius.

2. *p-i-n* type flexible hybrid perovskite solar cells

The *p-i-n* type flexible hybrid perovskite solar cells have benefit for fabricating flexible hybrid perovskite solar cells because the ETL can be formed at low temperature ($<$ 100 °C) solution process. Phenyl-C61-butyric acid methyl ester (PCBM), one of the fullerene derivatives, is well known as an *n*-type material for conventional organic solar cells, and has already been utilized in the *p-i-n* type devices [85–92]. The PCBM layer deposited on the perovskite effectively protects the trap states and reduce the infamous photocurrent hysteresis. Carmona *et al.* reported the flexible hybrid perovskite solar cells constructed to PET/TCO/PEDOT:PSS/hybrid perovsksite/PCBM/Au as shown in Fig. 9 [93]. The J-V characteristics of a flexible perovskite solar cell with a typical small area (0.12 cm^2) measured under 1 sun showed 14.3 mA/cm^2 J_{sc}, 1.04 V V_{oc}, 47% FF, and 7% PCE. The reduction of FF and PCE is due to thick holes and electronic blocking layers on flexible substrates. This can be avoided when large substrates are used in a batch or roll-to-roll process. The solar cell also has a slight decrease in PCE of 0.1% after 50 cycles of 5.5 mm in diameter bending. An inverted flexible perovskite slide cells with PEDOT:PSS as the hole selection contact and the PCBM layer as the *n*-type contact was developed by Docampo *et al.* [87]. In order to confirm the possibility of an *p-i-n* inverted perovskite solar cell, a solar cell structure was fabricated on FTO/glass substrate. As a result, the *p-i-n* structure achieved 16 mA/cm J_{sc}, 0.9 V V_{oc}, 66% FF, and 9.8% PCE. (Fig. 10) The main difference between these two device structures is the annealing of the TiO_2 layer at 500 °C in a *n-i-p* structures device. To make sure that this could affect device performance, they fabricated the usual ones with a small non-sintered TiO_x layer and noted the same reduction in all photovoltaic performance parameters, especially FF. These results led to the conclusion that the inverted

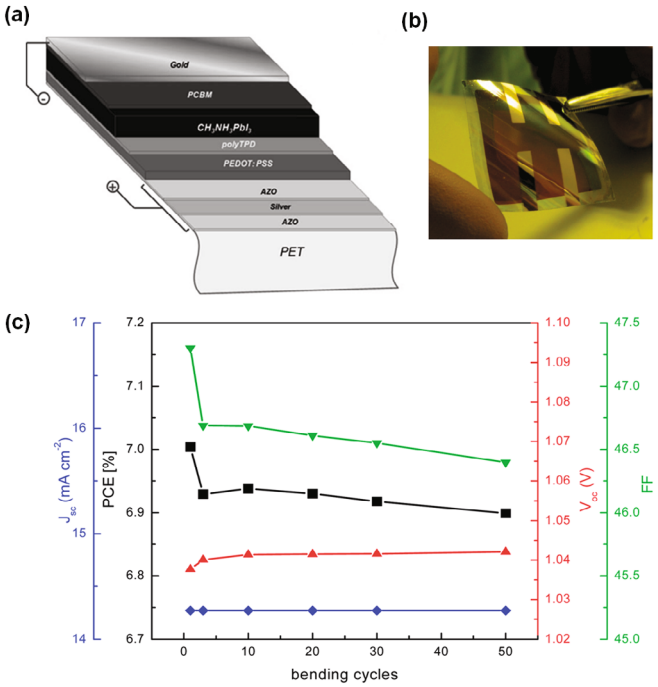

Fig. 9. (Color online) (a) Schematic layout of the flexible perovskite solar cell (b) Photograph of the flexible solar cell. (c) PCE, FF, J_{sc}, and V_{oc} for various of bending cycles. Reprinted from Ref. [93].

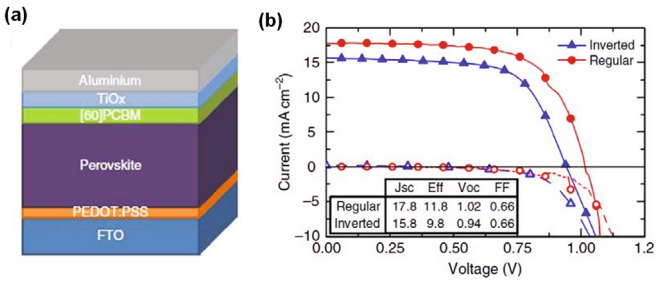

Fig. 10. (Color online) (a) Schematic device inverted structure (FTO/PEDOT:PSS/$MAPbI_{3-x}Cl_x$/PCBM /TiO_x/Al). (b) J-V curves for best devices of regular mesosuperstructured solar cells (red circles) and inverted planar-heterojunction (blue triangles) configuration. Inset: Photovoltaic parameters for both device architectures. Reprinted from Ref. [87].

perovskite solar cell structure should achieve the same efficiency as the highest performance general-purpose device when a properly effective TiO_x or air-stable n-type collector layer is used. In addition, You *et al.* fabricated an inverted flexible mixed halide perovskite solar cell using PCBM as the ETL [88]. As a results, a PCE of 11.5% was obtained on a ITO/glass rigid substrate and a PCE of 9.2% was achieved on a ITO/PET flexible substrate. In this study, PL and time-resolved photoluminescence (TRPL) were measured to observe charge generation in a perovskite photovoltaic cell. The PL results showed that a significant quenching effect occurs

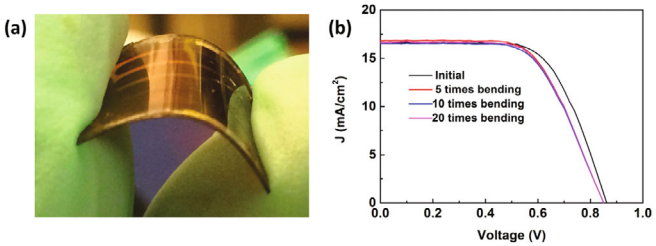

Fig. 11. (Color online) (a) Actual image of flexible perovskite solar cells on PET/ITO substrate. (b) device performance of the perovskite solar cells on PET/ITO flexible substrate before and after bending cycles. Reprinted from Ref. [89].

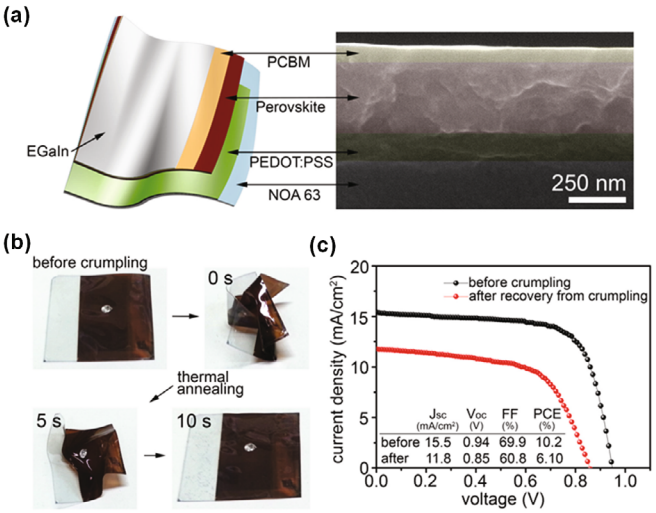

Fig. 12. (Color online) (a) Device architecture of the ultra-flexible perovskite solar cell on an NOA 63 film and a cross-sectional SEM image of the device (b) Photographs showing the state of device during the crumpling test. (c) J-V curves measured before crumpling and after shape recovery from crumpling test. Reprinted from Ref. [94].

when the perovskite layer contacts the PEDOT: PSS or PCBM layer. The PCBM-coated perovskite films show that PL is fully quenched, and PEDOT:PSS-based samples represent approximately 10% PL, indicating charge generation at both interfaces. It can be seen that the carrier generation at the perovskite/PEDOT:PSS interface is slightly less than at the perovskite/PCBM interface. In order to further confirm this charge transport process, TRPL measurements were performed and the PL lifetime was as high as 200.1 ns, consistent with previous reports [51]. This long lifetime requires longer exciton/carrier diffusion lengths needed to thicken the film for light harvesting. For example, for PEDOT:PSS/perovskite, the lifetime is reduced to 50 ns, and when the PCBM layer is coated on the perovskite layer, the carrier lifetime is further reduced to 25.4 ns. This indicates that charge transfer from perovskite to PCBM can be faster than PEDOT:PSS. This powerful PL quenching occurs with fast charge transfer at the interface, which can be

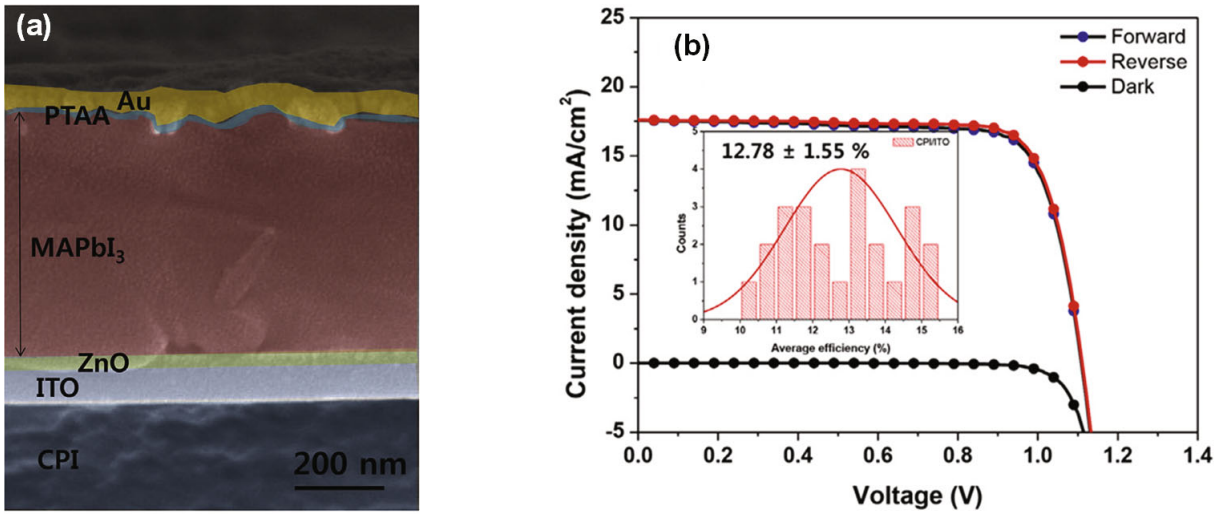

Fig. 13. (Color online) (a) Representative cross-sectional FESEM image of flexible $MAPbI_3$ perovskite solar cell (b) J-V curves of flexible $MAPbI_3$ perovskite solar cells comprised of Au/PTAA/$MAPbI_3$/ZnO/ITO/CPI substrate. Inset: PCE deviations of 24 samples. Reprinted from Ref. [95].

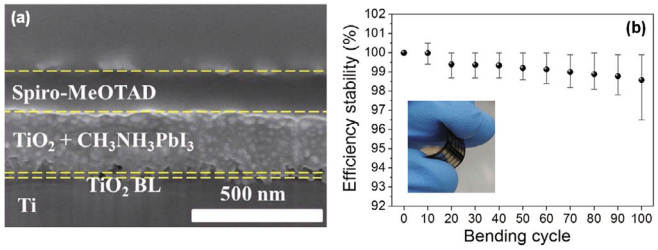

Fig. 14. (Color online) (a) Cross-sectional image of $MAPbI_3$ perovskite solar cell using a Ti substrate with ultra-thin metal film. (b) PCE stability of the flexible perovskite solar cells with Ti substrate. Evolution of J-V curves throughout 100 bending cycles Inset: real image during bend test. Reprinted from Ref. [31].

a charge separation and collection mechanism in these devices. The photovoltaic performance of the flexible device was 80% of the rigid device performance with 0.86V V_{oc}, 16.5 $mAcm^{-2}$ J_{sc}, 64% FF, and 9.2% PCE. The mechanical bend test shows that the machine is slightly reduced in performance by bending up to 20 times. (see Fig. 11) In addition, Park *et al.* demonstrate that can recover the complete shape of a perovskite solar cell device after crumpling using noland optical adhesive (NOA) 63 substrate, which is a form-recoverable polymer. (see Fig. 12) [94]. These results show that the use of flexible electrodes prevents mechanical damage to the perovskite layer and the PCE before and after bending at a radius of 1 mm is measured as 10.75% and 10.4%, respectively. The shape recoverable perovskite solar with NOA 63 substrate also shows a PCE of 6.07% after crumpling.

Most recently, Park *et al.* fabricated a flexible $MAPbI_3$ perovskite solar cell using a roll-to-roll sputtered ITO film on a colorless polyimide (CPI) substrate 60 mm thick, as shown in Fig. 13 [95]. As a results, flexible perovskite solar cells with the structure of Au/PTAA/$MAPbI_3$/ ZnO/ITO/CPI showed a high PCE of 15.5%. It also shows that at a radius of curvature = 2 mm, it maintains more than 90% of its original efficiency.

V. TCO-FREE TCE BASED FLEXIBLE HYBRID PEROVSKITE SOLAR CELLS

1. Thin metal TCE based flexible hybrid perovskite solar cells

Application of ITO or FTO to a flexible substrate has many disadvantages such as cracking of the ITO or FTO layer upon device bending, chemical instability under acidic or basic conditions, and degradation of device performance due to the high cost of indium. Therefore, devices with ITO electrodes are unsuitable for providing cost-effective, flexible systems. Metal substrates are one of the candidate materials to replace expensive ITO [96]. Although the metal substrate acts as both of flexible substrate and conductor, the light cannot transmit the metal substrate. Therefore, a transparent counter electrode is required to transmit the external light into the solar cells. Recently, Lee *et al.* fabricated a solar cell with an Ag/spiro-MeOTAD/$MAPbI_3$/mesoporous TiO_2/dense TiO_2/Ti electrode structure using an ultra-thin film of transparent silver on top, as shown in Fig. 14 [31]. In this study they measured the transmittance spectrum of the film with Ag thickness to determine the amount of light passing through the ultra thin film. As the thickness of the Ag film increased from 8 nm to 20 nm, it was found that the intensity of the transmitted

Table 5. Average photovoltaic parameters of perovskite solar cells on Ti substrates at different Ag thicknesses measured under AM 1.5G illumination. (Parenthesis represents highest value) Reprinted from Ref. [31].

Ag thickness (nm)	V_{oc} (V)	J_{sc} (mA/cm^2)	FF (%)	PCE (%)
8	0.766 ± 0.064 (0.865)	2.97 ± 1.28 (5.30)	0.21 ± 0.04 (0.30)	0.46 ± 0.18 (0.77)
12	0.855 ± 0.023 (0.903)	7.04 ± 1.74 (9.50)	0.68 ± 0.05 (0.75)	4.07 ± 1.08 (6.15)
16	0.835 ± 0.045 (0.889)	5.45 ± 1.00 (6.50)	0.59 ± 0.05 (0.68)	2.70 ± 0.66 (3.85)
20	0.756 ± 0.061 (0.846)	4.53 ± 0.94 (6.10)	0.58 ± 0.08 (0.69)	2.03 ± 0.65 (2.99)

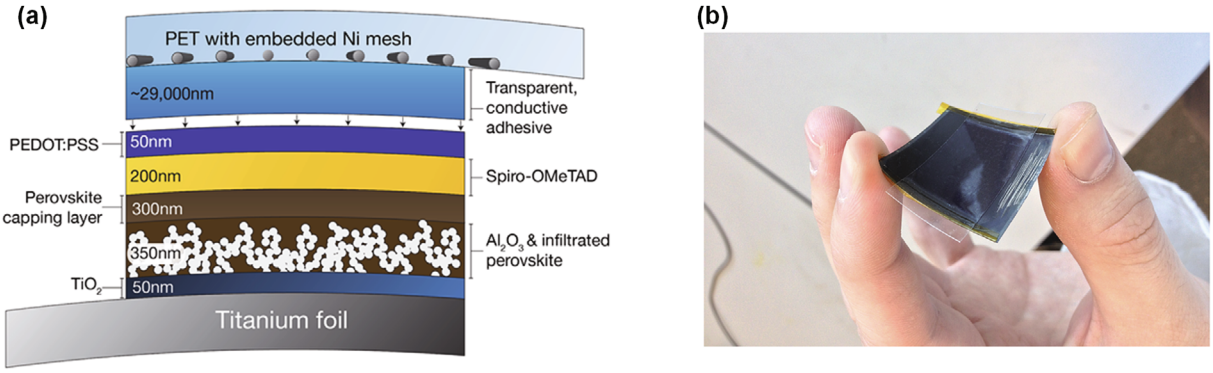

Fig. 15. (Color online) (a) Schematic representation of a metal mounted perovskite solar cell and associated target layer thicknesses. (b) Photograph image of a flexible perovskite solar cell on Ti foil. Reprinted from Ref. [97].

light was significantly reduced by absorbing more light. The device showed a maximum efficiency of 6.15% at 12 nm-thick Ag film, but above 12 nm, the efficiency decreases to 2.03%, as summarized in Table 5. This clearly shows that the thickness of the Ag layer controls the number of photons. In order to check the importance of the Ti substrate, we measured the J-V curves with/without Ti substrate, respectively. The solar cell with the Ti substrate showed a slightly higher J_{sc} (9.8 mA cm^{-2}) than the device without the Ti substrate (9.2 mAcm^{-2}). This result can be regarded as an increase in light due to reflection by the Ti substrate. In addition, PCE reduces only 1.5% of the original value after 100 bending cycles at bending curvature radius of 4 mm, which is superior to ITO-based flexible perovskite solar cells for roll-to-roll processing. In addition, Troughton *et al.* fabricated a indium-free, plastic-free perovskite solar cell with a PCE of 10.3% using a Ti foil as a substrate and a transparent conductive adhesive (TCA) as a counter electrode to a PET film coated with a Ni grid [97]. Figure 15 shows a schematic view of the perovskite solar cell using metal foil substrate and real image. They play an important role in transporting charge from hole transport material (HTM) to small 'islands' of PEDOT:PSS in TCA by adopting PEDOT:PSS interlayer spray in HTM. They found that the effect of this interlayer could dramatically increase the J_{sc} and FF of the solar cell, ultimately increasing the efficiency of the device.

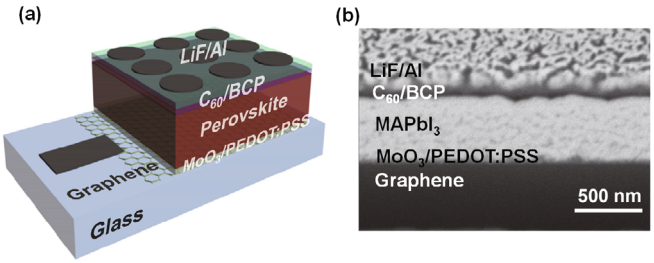

Fig. 16. (Color online) (a) Schematic structure of the inverted $MAPbI_3$ perovskite solar cells utilizing graphene as a transparent anode. (b) Cross-sectional SEM images of the devices employing graphene/2 nm MoO_3 electrode. Reprinted from Ref. [103].

2. Graphene TCE based flexible hybrid perovskite solar cells

To date, flexible solar cell research has been reported in the field of organic photovoltaics using electrodes such as graphene and carbon nanotubes [98–101]. Among them, the graphene electrode is one of the promising TCE candidates for the next generation perovskite solar cell due to its high transmittance in the visible light near infrared region, excellent flexibility, excellentchemical stability and easy adjustment of the Fermi level by doping [102]. In addition, in order to extract all the charge carriers generated in the active layer with TCE, the TCE must be covered in the entire area of the substrate without pinholes. Therefore, graphene elec-

Table 6. Photovoltaic parameters of the graphene- or ITO-based flexible perovskite solar cell devices with MoO_3 layers of varying thickness. Reprinted from Ref. [103].

Sample ID	Electrode	MoO_3 thickness (nm)	V_{oc} (V)	J_{sc} (mA/cm^2)	FF (%)	PCE (%)	Best PCE (%)
G-M1	Graphene	1	0.72 ± 0.36	17.6 ± 6.3	0.45 ± 0.09	6.7 ± 4.2	12.1
G-M2		2	1.03 ± 0.02	21.9 ± 0.4	0.72 ± 0.02	16.1 ± 0.6	17.1
G-M4		4	1.00 ± 0.01	22.9 ± 0.4	0.70 ± 0.02	15.9 ± 0.5	16.2
ITO-M0	ITO	0	0.96 ± 0.01	21.4 ± 0.5	0.83 ± 0.02	17.0 ± 0.4	17.6
ITO-M1		1	0.97 ± 0.01	22.6 ± 0.4	0.83 ± 0.01	18.2 ± 0.5	18.8
ITO-M2		2	0.95 ± 0.01	22.2 ± 0.4	0.76 ± 0.01	16.1 ± 0.4	16.9
ITO-M4		4	0.94 ± 0.01	21.0 ± 0.4	0.74 ± 0.01	14.7 ± 0.6	15.7

Table 7. Photovoltaic parameters in the forward and reverse scans and diffusion length (L_n) for the $MAPbI_3$ perovskite solar cells with undoped and doped graphene electrodes. Reprinted from Ref. [107].

Sample ID	Charge carrier density (cm^{-3})	Scan Direction	V_{oc} (V)	J_{sc} (mA/cm^2)	FF (%)	PCE (%)	L_n (nm)
Pristine	1.42×10^{18}	Forward	1.03	19.5	57.5	11.5	~ 210
		Reverse	1.04	19.6	61.8	12.6	
1 mM	3.81×10^{18}	Forward	1.05	22.1	66.0	15.4	~ 260
		Reverse	1.06	22.2	67.6	15.9	
2.5 mM	5.70×10^{18}	Forward	1.06	21.8	70.1	16.2	~ 290
		Reverse	1.07	21.8	72.1	16.8	
5 mM	7.94×10^{18}	Forward	1.08	21.4	74.7	17.3	~ 350
		Reverse	1.08	21.5	76.7	17.8	
7.5 mM	9.13×10^{18}	Forward	1.08	21.0	76.6	17.4	~ 370
		Reverse	1.09	21.0	78.3	17.9	
10 mM	1.31×10^{19}	Forward	1.08	20.4	75.6	16.7	~ 360
		Reverse	1.08	20.4	77.6	17.1	

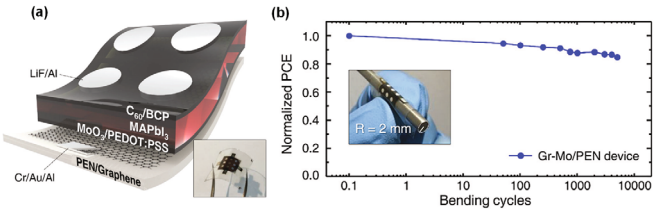

Fig. 17. (Color online) (a) Device structure of graphene-based flexible perovskite solar cells. Inset: Photograph of a complete device. (b) Bending stability test under harsh conditions. The normalized PCE of the $MAPbI_3$ perovskite with MoO_3 doped graphene/PEN device as a function of bending cycles with a fixed bending radius = 2 mm. Reprinted from Ref. [104].

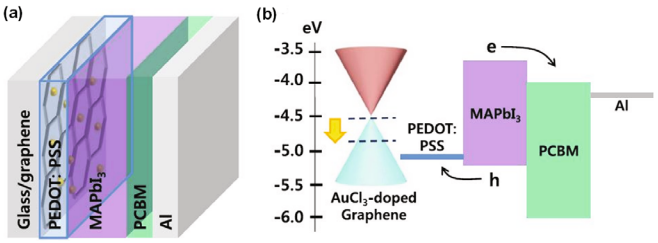

Fig. 18. (Color online) (a) Schematic *p-i-n*-type planar $MAPbI_3$ perovskite solar cell device structure (b) Energy band diagram of a $MAPbI_3$ perovskite solar cell composed of glass/$AuCl_3$-doped (or undoped) graphene /PEDOT:PSS/$MAPbI_3$/PCBM/Al. Yellow arrow indicates the shift of Fermi level of graphene by $AuCl_3$ doping. Reprinted from Ref. [107].

trode are suitable for solar cell TCE, but Ag nanowires, Ag networks, and carbon nanotubes are unsuitable because they cannot cover the entire surface of the substrate. Recently, Sung, *et al.* has succeeded to fabricate 17.1% *p-i-n*-type TCO-free perovskite solar cells without hysteresis by using molybdenum trioxide (MoO_3)-doped single-layer graphene/glass substrate as a transparent conductive anode instead of ITO as shown in Fig. 16 [103]. In particular, MoO_3 works better as a conductive electrode by doping holes in graphene. With an optimized thickness of the MoO_3 layer, the perovskite solar cell was achieved best PCE of 17.1% and 18.8% for graphene and ITO TCE, as summarized in Table 6. However, the conductivity of the graphene electrode was much lower than that of the ITO electrode, resulting in

lower efficiency, but the J_{sc} and V_{oc} were increased due to the high transparency and low surface roughness of graphene. In addition, they also demonstrate super flexible perovskite solar cells using MoO_3-doped graphene TCE. The best efficiency of the graphene TCE-based perovskite device was 17.3% and the PCE of the corresponding ITO electrode was 16.8% [104]. In addition, the flexible device maintains more than 80% of its original efficiency even after 5,000 bend cycles with a curvature radius = 2 mm, demonstrating excellent stability against bending deformation.(see Fig. 17) Very recently, Heo *et al.* reported a high-efficiency perovskite solar cell by controlling the sheet resistance and work function of graphene by a simple chemical doping technique under ambient conditions. Gold chloride ($AuCl_3$) is known to be a *p*-type dopant for graphene [102,105,106]. In this study, Heo ea al. first realize high-efficiency TCO-free perovskite solar cells with *p*-type-graphene TCEs engineered by $AuCl_3$ doping. (see Fig. 18) [107] $AuCl_3$ powder was dissolved in nitromethane at concentrations (n_D) of 1, 2.5, 5, 7.5, and 10 mM for preparing $AuCl_3$ doping solution. With increasing n_D, the sheet resistance of the $AuCl_3$-doped graphene significantly decreases down to $\sim$ 70 ohm/sq, much smaller than that of pristine graphene ($\sim$ 890 ohm/sq). However, the transmittance of the $AuCl_3$-doped graphene is gradually degraded with increasing n_D. Due to the n_D-dependent trade-off correlation between the sheet resistance and the transmittance of the $AuCl_3$-doped graphene, the ratio of DC conductivity/optical conductivity is highest at $n_D = 7.5$ mM, resulting in the highest PCE of 17.9%, as summarized in Table 7. These results suggest that perovskite solar cells with graphene transparent electrodes provide new insights into future research to develop efficient and flexible solar cells.

VI. SUMMARY AND OUTLOOK

We reviewed recent advances of TCO and TCO-free substrate based flexible hybrid perovskite solar cells. The ITO TCO is generally used to flexible hybrid solar cells with *n-i-p* or *p-i-n* device architecture. For flexible TCO-free substrate, the conducting polymer, metal mesh, and doped graphene TCE or Ti metal substrate have been adapted to date. Currently, the efficiency drops between ITO/glass based rigid hybrid perovskite solar cells and ITO based flexible hybrid solar cells are 10% due to the reduced transmission of ITO/flexible substrate compared to ITO/glass substrate. If the flexible substrates with similar refractive index to glass and/or new TCE such as graphene with higher transmittance and comparable/better sheet resistance than the ITO TCO are successfully developed, the flexible hybrid perovskite solar cells will have similar or better performance than the rigid TCO based devices. Currently, the record power conversion efficiency of rigid TCO based hybrid perovskite solar cells is over 22%. Therefore, the flexible hybrid perovskite solar cells with over 20% efficiency will be demonstrated in near future, although current efficiency of flexible hybrid solar cells is > 17% at 1 Sun. To optimize the efficiency and flexibility of hybrid flexible perovskite solar cells, the flexible substrate, transparent electrode, and low temperature solution processable *n*-type or *p*-type charge transporting materials should be considered. To improve the device stability, the barrier films or sealant against water and oxygen invasion should also be developed. In addition, the large scale coating process such as roll-to-roll, slot-die, and spray for modularization should be developed. Furthermore, the Pb-free perovskite materials with high efficiency and flexibility should be developed in order to apply the flexible hybrid perovskite solar cells in human-friendly circumstance such as windows, mobile device charger, small electric appliances, and wearable device chargers. Currently, all above issues have been intensively studying independently in whole country. So I expect that super flexible, highly efficient hybrid perovskite solar modules will be demonstrated by integration of the key independent technologies in near future.

ACKNOWLEDGMENTS

This study was supported by the National Research Foundation of Korea (NRF) under the Ministry of Science, ICT & Future Planning (Basic Science Research Program (No.2014R1A5A1009799), Technology Development Program to Solve Climate Change (No. 2015M1A2A2055631) and Global Frontier R&D Program on Center for Multiscale Energy System (No. 2012M3A6A7054855)) and the Ministry of Trade, Industry & Energy, Republic of Korea (New & Renewable Energy Core Technology Program of the Korea Institute of Energy Technology Evaluation and Planning (KETEP) (No. 20163010012470)).

REFERENCES

[1] M. A. Green, Semicond. Sci. Technol. **8**, 1 (1993).
[2] J. Hupkes, B. Rech, O. Kluth, T. Repmann, B. Zwaygardt, J. Muller, R. Drese and M. Wuttig, Sol. Energy Mater. Sol. Cells **90**, 3054 (2006).
[3] J. Li, H. Y. Yu and Y Li, Nanoscale **3**, 4888 (2011).
[4] B-R. Huang, Y-K. Yang and W-L. Yang, Nanotechnology **25**, 035401 (2014).
[5] J. Britt and C. Ferekides, Appl. Phys. Lett. **62**, 2851 (1993).
[6] I. Repins, M. A. Contreras, B. Egaas, C. DeHart, J. Scharf, C. L. Perkins, B. To and R. Noufi, Prog. Photovolt.: Res. Appl. **16**, 235 (2008).
[7] C. W. Tang, Appl. Phys. Lett. **48**, 183 (1986).
[8] B. O'Regan and M. Gratzel, Nature **353**, 737 (1991).

[9] J. J. M. Halls, C. A. Walsh, N. C. Greenham, E. A. Marsegila, R. H. Frlend, S. C. Morattl and A. B. Holmes, Nature **376**, 498 (1995).
[10] R. W. Miles, G. Zoppi and I. Forbes, Mater. Today **10**, 21 (2007).
[11] S. P. Singh, CH. P. Kumar, G. D. Sharma, R. Kurchania and M. S. Roy, Adv. Funct. Mater. **22**, 4087 (2012).
[12] S. P. Singh, M. S. Roy, K. R. J. Thomas, S. Balaiah, K. Bhanuprakash and G. D. Sharma, J. Phys. Chem. C **116**, 5941 (2012).
[13] Q. Xue, Z. Hu, C. Sun, Z. Chen, F. Huang, H-L. Yip and Y. Cao, RSC Adv. **5**, 775 (2015).
[14] M. Liu, M. B. Johnston and H. J. Snaith, Nature **501**, 395 (2013).
[15] J. Burschka, N. Pellet, S-J. Moon, R. Humphry-Baker, P. Gao, M. K. Nazeeruddin and M. Gratzel, Nature **499**, 316 (2013).
[16] N. J. Jeon, J. H. Noh, W. S. Yang, Y. C. Kim, S. Ryu, J. Seo and S. I. Seok, Nature **517**, 476 (2015).
[17] H. Zhou, Q. Chen, G. Li, S. Luo, T-b. Song, H-S. Duan, Z. Hong, J. You, Y. Liu and Y Yang, Science **345**, 542 (2014).
[18] W. S. Yang, B-W. Park, E. H. Jung, N. J. Jeon, Y. C. Kim, D. U. Lee, S. S. Shin, J. Seo, E. K. Kim, J. H. Noh and S. I. Seok, Science **356**, 1376 (2017).
[19] B. O'Regan, D. T. Schwartz, S. M. Zakeeruddin and M. Grätzel, Adv. Mater. **12**, 1263 (2000).
[20] H-S. Kim, C-R. Lee, J-H. Im, K-B. Lee, T. Moehl, A. Marchioro, S-J. Moon, R. Humphry-Baker, J-H. Yum, J. E. Moser, M. Gratzel and N-G. Park, Sci. Rep. **2**, 591 (2012).
[21] M. M. Lee, J. Teuscher, T. Miyasaka, T. N. Murakami and H. J. Snaith, Science **338**, 643 (2012).
[22] Y. Ogomi, A. Morita, S. Tsukamoto, T. Saitho, Q. Shen, T. Toyoda, K. Yoshino, S. S. Pandey, T. Ma and S. Hayase, J. Phys. Chem. C **118**, 16659 (2014).
[23] J. A. Christians, R. C. M. Fung and P. V. Kamat, J. Am. Chem. Soc. **136**, 758 (2014).
[24] Z. Fan and A. Javey, Nature Mater. **7**, 835 (2008).
[25] J. Yoon, A. J. Baca, S-I. Park, P. Elvikis, J. B. Geddes III, L. Li, R. H Kim, J. Xiao, S. Wang, T-H Kim, M. J. Motala, B. Y. Ahn, E. B. Duoss, J. A. Lewis, R. G. Nuzzo, P. M. Ferreira, Y. Huang, A Rockett and J. A. Rogers, Nature Mater. **7**, 907 (2008).
[26] J-Y. Lee, S. T. Connor, Y. Cui and P. Peumans, Nano Lett. **8**, 689 (2008).
[27] Y. Galagan, J-E. J. M. Rubingh, R. Andriessen, C-C. Fan, P. W. M. Blom, S. C. Veenstra and J. M. Kroon, Sol. Energy Mater. Sol. Cells **95**, 1339 (2011).
[28] S. Chu, D. Li, P-C. Chang and J. G Lu, Nanoscale Res. Lett. **6**, 38 (2011).
[29] X. Feng, K. Singh, S. Bhavanam, V. Palekis, D. L. Morel and C. Ferekides, Thin Solid Films **535**, 202 (2013).
[30] R. Wuerz, A. Eicke, F. Kessler, S. Paetel, S. Efimenko and C. Schlegel, Sol. Energy Mater. Sol. Cells **100**, 132 (2012).
[31] M. Lee, Y Jo, D. S. Kim and Y. Jun, J. Mater. Chem. A **3**, 4129 (2015).
[32] J. Yang, A. Banerjee and S. Guha, Appl. Phys. Lett. **70**, 2975 (1997).
[33] F. Zhang, M. Johansson, M. R. Andersson, J. C. Hummelen and O. Inganas, Adv. Mater. **14**, 662 (2002).
[34] W. U. Huynh, J. J. Dittmer and A. P. Alivisatos, Science **295**, 2425 (2002).
[35] T. Aernouts, P. Vanlaeke, W. Geens, J. Poortmans, P. Heremans, S. Borghs, R. Mertens, R. Andriessen and L. Leenders, Thin Solid Films **451-452**, 22 (2004).
[36] M. B. Schubert and J. H. Werner, Mater. Today **9**, 42 (2006).
[37] D. Wever, Z. Naturforsch. **33b**, 1443 (1978).
[38] D. Weber, Z. Naturforsch. **33b**, 862 (1978).
[39] D. B. Mltzl, C. A. Felld, W. T. A. Harrison and A. M. Guloy, Nature **369**, 467 (1994).
[40] C. R. Kagan, D. B. Mitzi and C. D. Dimitrakopoulos, Science **286**, 945 (1999).
[41] A. Kojima, M. Ikegami, K. Teshima and T. Miyasaka, Chem. Lett. **41**, 397 (2012).
[42] V. M. Goldschmidt, Ber. Dtsch. Chem. Ges. **60**, 1263 (1927).
[43] M. Johnsson and P. Lemmens, *Handbook of Magnetism and Advanced Magnetic Materials* (John Wiley & Sons, Ltd., 2007).
[44] Z. Fan, K. Sunc and J. Wang, J. Mater. Chem. A **3**, 18809 (2015).
[45] J. H. Heo, S. H. Im, J. H. Noh, T. N. Mandal, C-S. Lim, J. A. Chang, Y. H. Lee, H-j. Kim, A. Sarkar, M. K. Nazeeruddin, M. Grätzel and S. I. Seok, Nature Photon. **7**, 486 (2013).
[46] J. H. Noh, S. H. Im, J. H. Heo, T. N. Mandal and S. I. Seok, Nano Lett. **13**, 1764 (2013).
[47] A. Kojima, K. Teshima, Y. Shirai and T. Miyasaka, J. Am. Chem. Soc. **131**, 6050 (2009)
[48] L. Etgar, P. Gao, Z. Xue, Q. Peng, A. K. Chandiran, B. Liu, Md. K. Nazeeruddin and M. Gratzel, J. Am. Chem. Soc. **134**, 17396 (2012).
[49] J. M. Frost, K. T. Butler, F. Brivio, C. H. Hendon, M. van Schilfgaarde and A. Walsh, Nano Lett. **14**, 2584 (2014).
[50] C. Bernal and K. Yang, J. Phys. Chem. C **118**, 24383 (2014).
[51] S. D. Stranks, G. E. Eperon, G. Grancini, C. Menelaou, M. J. P. Alcocer, T. Leijtens, L. M. Herz, A. Petrozza and H. J. Snaith, Science **342**, 341 (2013).
[52] A. Dualeh, T. Moehl, N. Tetreault, J. Teuscher, P. Gao, M. K. Nazeeruddin and M. Gratzel, ACS Nano **8**, 362 (2014).
[53] G. Giorgi, J-I. Fujisawa, H. Segawa and K. Yamashita, J. Phys. Chem. Lett, **4**, 4213 (2013).
[54] C. S. Ponseca Jr., T. J. Savenije, M. Abdellah, K. Zheng, A. Yartsev, T. Pascher, T. Harlang, P. Chabera, T. Pullerits, A. Stepanov, J-P. Wolf and V. Sundström, J. Am. Chem. Soc. **136**, 5189 (2014).
[55] J. Qiu, Y. Qiu, K. Yan, M. Zhong, C. Mu, H. Yan and S. Yang, Nanoscale **5**, 3245 (2013).
[56] B-W. Park, B. Philippe, S. M. Jain, X. Zhang, T. Edvinsson, H. Rensmo, B. Zietza and G. Boschloo, J. Mater. Chem. A **3**, 21760 (2015).
[57] E. Mosconi, A. Amat, M. K. Nazeeruddin, M. Graätzel and F. D. Angelis, J. Phys. Chem. C **117**, 13902 (2013).
[58] S. D. Wolf, J. Holovsky, S-J. Moon, P. Löper, B. Niesen, M. Ledinsky, F-J. Haug, J-H. Yum and C. Ballif, J. Phys. Chem. Lett. **5**, 1035 (2014).
[59] H-S. Kim, S. H. Im and N-G. Park, J. Phys. Chem. C **118**, 5615 (2014).
[60] G. Xing, N. Mathews, S. Sun, S. S. Lim, Y. M. Lam,

M. Grätzel, S. Mhaisalkar and T. C. Sum, Science **342**, 344 (2013).
[61] J-H. Im, C-R. Lee, J-W. Lee, S-W. Park and N-G. Park, Nanoscale **3**, 4088 (2011).
[62] S. S. Shin, E. J. Yeom, W. S. Yang, S. Hur, M. G. Kim, J. Im, J. Seo, J. H. Noh and S. I. Seok, Science **356**, 167 (2017).
[63] W. S. Yang, J. H. Noh, N. J. Jeon, Y. C. Kim, S. Ryu, J. Seo and S. I. Seok, Science **348**, 1234 (2015).
[64] P. Du, X. Hu, C. Yi, H. C. Liu, P. Liu, H-L. Zhang and X. Gong, Adv. Funct. Mater. **25**, 2420 (2015).
[65] L. Qiu, J. Deng, X. Lu, Z. Yang and H. Peng, Angew. Chem. Int. Ed. **53**, 10425 (2014).
[66] B. J. Kim, D. H. Kim, Y-Y. Lee, H-W. Shin, G. S. Han, J. S. Hong, K. Mahmood, T. K. Ahn, Y-C. Joo, K. S. Hong, N-G. Park, S. Lee and H. S. Jung, Enegy Environ. Sci. **8**, 916 (2015).
[67] Y. Li, L. Meng, Y. Yang, G. Xu, Z. Hong, Q. Chen, J. You, G. Li, Y. Yang and Y. Li, Nature Commun. **7**, 10214 (2016).
[68] T. M. Brown, F. De Rossi, F. D. Giacomo, G. Mincuzzi, V. Zardetto, A. Realea and A. D. Carloa, J. Mater. Chem. A **2**, 10788 (2014).
[69] N. S. Lewis, Science **315**, 798 (2007).
[70] V. Zardetto, G. Mincuzzi, F. D. Rossi, F. D. Giacomo, A. Reale, A. D. Carlo and T. M. Brown, Appl. Energy **113**, 1155 (2014).
[71] M. Grätzel, Nature Mater. **13**, 838 (2014).
[72] N. J. Jeon, H. G. Lee, Y. C. Kim, J. Seo, J. H. Noh, J. Lee and S. I. Seok, J. Am. Chem. Soc. **136**, 7837 (2014).
[73] T. Leijtens, G. E. Eperon, S. Pathak, A. Abate, M. M. Lee and H. J. Snaith, Nature Commun. **4**, 2885 (2013).
[74] C. Law, L. Miseikis, S. Dimitrov, P. Shakya-Tuladhar, X. Li , P. R. F. Barnes, J. Durrant and B. C. O'Regan, Adv. Mater. **26**, 6268 (2014).
[75] A. Mei, X. Li, L. Liu, Z. Ku, T. Liu, Y. Rong, M. Xu, M. Hu, J. Chen, Y. Yang, M. Grätzel and H. Han, Science **345**, 295 (2014).
[76] H. B. Profijt, S. E. Potts, M. C. M. van de Sanden and W. M. M. Kesselsa, J. Vac. Sci. Technol. A **29**, 050801 (2011).
[77] F. D. Giacomo, V. Zardetto, A. D'Epifanio, S. Pescetelli, F. Matteocci, S. Razza, A. D. Carlo, S. Licoccia, W. M. M. Kessels, M. Creatore and T. M. Brown, Adv. Energy Mater. **5**, 1401808 (2015).
[78] B. J. Kim, D. H. Kim, Y-Y. Lee, H-W. Shin, G. S. Han, J. S. Hong, K. Mahmood, T. K. Ahn, Y-C. Joo, K. S. Hong, N-G. Park, S. Lee and H. S. Jung, Energy Environ. Sci. **8**, 916 (2015).
[79] Q. Zhang, C. S. Dandeneau, X. Zhou and G. Cao, Adv. Mater. **21**, 4087 (2009).
[80] J. B. Baxter and E. S. Aydil, Appl. Phys. Lett. **86**, 053114 (2005).
[81] I. Gonzalez-Valls and M. Lira-Cantu, Energy Environ. Sci. **2**, 19 (2009).
[82] M. H. Kumar, N. Yantara, S. Dharani, M. Graetzel, S. Mhaisalkar, P. P. Boix and N. Mathews, Chem Commun. **49**, 11089 (2013).
[83] D. Liu and T. L. Kelly, Nature Photon. **8**, 133 (2014).
[84] J. H. Heo, M. H. Lee, H. J. Han, B. R. Patil, J. S. Yub and S. H. Im, J. Mater. Chem. A **4**, 1572 (2016).
[85] J-Y. Jeng, Y-F. Chiang, M,-H. Lee, S-R. Peng, T-F. Guo, P. Chen and T-C. Wen, Adv. Mater. **25**, 3727 (2013).
[86] S. Sun, T. Salim, N. Mathews, M. Duchamp, C. Boothroyd, G. Xing, T. C. Sum and Y. M. Lam, Energy Environ. Sci. **7**, 399 (2014).
[87] P. Docampo, J. M. Ball, M. Darwich, G. E. Eperon and H. J. Snaith, Nature Commn. **4**, 2761 (2013).
[88] O. Malinkiewicz, A. Yella, Y. H. Lee, G. M. Espallargas, M. Graetzel, M. K. Nazeeruddin and H. J. Bolink, Nature Photon. **8**, 128 (2014).
[89] J. You, Z. Hong, Y. (Michael) Yang, Q. Chen, M. Cai, T-B. Song, C-C. Chen, S. Lu, Y. Liu, H. Zhou and Y Yang, ACS Nano **8**, 1674 (2014).
[90] J. Seo, S. Park, Y. C. Kim, N. J. Jeon, J. H. Noh, S. C. Yoon and S. I. Seok, Energy Environ. Sci. **7**, 2642 (2014).
[91] Q. Wang, Y. Shao, Q. Dong, Z. Xiao, Y. Yuan and J Huang, Energy Environ. Sci. **7**, 2359 (2014).
[92] Z. Xiao, Q. Dong, C. Bi, Y. Shao, Y. Yuan and J. Huang, Adv. Mater. **26**, 6503 (2014).
[93] C. Rold'an-Carmona, O. Malinkiewicz, A. Soriano, G. M. Espallargas, A. Garcia, P. Reinecke, T. Kroyer, M. I. Dar, M. K. Nazeeruddin and H. J. Bolink, Energy Environ. Sci. **7**, 994 (2014).
[94] M. Park, H. J. Kim, I. Jeong, J. Lee, H. Lee, H. J. Son, D-E. Kim and M. J. Ko, Adv. Energy Mater. **5**, 1501406 (2015).
[95] J-I. Park, J. H. Heo, S-H. Park, K. I. Hong, H. G. Jeong, S. H. Im and H-K. Kim, J. Power Source **341**, 340 (2017).
[96] S. K. Balasingam, M. G. Kangw and Y. Jun, Chem. Commun. **49**, 11457 (2013).
[97] J. Troughton, D. Bryant, K. Wojciechowski, M. J. Carnie, H. Snaith, D. A. Worsleya and T. M. Watson, J. Mater. Chem. A **3**, 9141 (2015).
[98] M. W. Rowell, M. A. Topinka, M. D. M-J. Prall, G. Dennler, N. S. S. Hu and G. Gruner, Appl. Phys. Lett. **88**, 233506 (2006).
[99] S. Cataldo, P. Salice, E. Menna and B. Pignataro, Energy Environ. Sci. **5**, 5919 (2012).
[100] Y. Wang, S. W. Tong, X. F. Xu, B. Özyilmaz and K. P. Loh, Adv. Mater. **23**, 1514 (2011).
[101] H. Park, S. Chang, X. Zhou, J. Kong, T. Palacios and S. Gradečak, Nano Lett. **14**, 5148 (2014).
[102] H-J. Shin, W. M. Choi, D. Choi, G. H. Han, S-M. Yoon, H-K. Park, S-W. Kim, Y. W. Jin, S. Y. Lee, J. M. Kim, J-Y. Choi and Y. H. Lee, J. Am. Chem. Soc. **132**, 15603 (2010).
[103] H. Sung, N. Ahn, M. S. Jang, J-K. Lee, H. Yoon, N-G. Park and M. Choi, Adv. Energy Mater. **6**, 1501873 (2016).
[104] J. Yoon, H. Sung, G. Lee, W. Cho, N. Ahn, H. S. Jung and M. Choi, Energy Environ. Sci. **10**, 337 (2017).
[105] D. H. Shin, S. Kim, J. M. Kim, C. W. Jang, J. H. Kim, K. W. Lee, J. Kim, S. D. Oh, D. H. Lee, S. S. Kang, C. O. Kim, S-H. Choi and K. J. Kim, Adv. Mater. **27**, 2614 (2015).
[106] C. W. Jang, J. M. Kim, J. H. Kim, D. H. Shin, S. Kim and S-H. Choi, Journal of Alloys & Compounds **621**, 1 (2015)
[107] J. H. Heo, D. H. Shin, S. Kim, M. H. Jang, M. H. Lee, S. W. Seo, S-H. Choi and S. H. Im, Chem. Eng. J. **323**, 153 (2017).